

The accurate measurement of spin orbit torque by utilizing the harmonic longitudinal voltage with Wheatstone bridge structure

Cite as: Appl. Phys. Lett. **116**, 222402 (2020); <https://doi.org/10.1063/1.5145221>

Submitted: 17 January 2020 • Accepted: 24 May 2020 • Published Online: 02 June 2020

Bo Wang, Yonghai Guo, Bo Han, et al.



View Online



Export Citation



CrossMark

ARTICLES YOU MAY BE INTERESTED IN

[Spin transfer torque devices utilizing the giant spin Hall effect of tungsten](#)

Applied Physics Letters **101**, 122404 (2012); <https://doi.org/10.1063/1.4753947>

[Spin-orbit torques: Materials, physics, and devices](#)

Applied Physics Letters **118**, 120502 (2021); <https://doi.org/10.1063/5.0039147>

[Spin-orbit torque characterization in a nutshell](#)

APL Materials **9**, 030902 (2021); <https://doi.org/10.1063/5.0041123>



Instruments for Advanced Science

- Knowledge
- Experience ■ Expertise

Click to view our product catalogue

Contact Hiden Analytical for further details:

www.HidenAnalytical.com
info@hiden.co.uk

Gas Analysis

- ▶ dynamic measurement of reaction gas streams
- ▶ catalysis and thermal analysis
- ▶ molecular beam studies
- ▶ dissolved species probes
- ▶ fermentation, environmental and ecological studies

Surface Science

- ▶ UHVTPD
- ▶ SIMS
- ▶ end point detection in ion beam etch
- ▶ elemental imaging - surface mapping

Plasma Diagnostics

- ▶ plasma source characterization
- ▶ etch and deposition process reaction kinetic studies
- ▶ analysis of neutral and radical species

Vacuum Analysis

- ▶ partial pressure measurement and control of process gases
- ▶ reactive sputter process control
- ▶ vacuum diagnostics
- ▶ vacuum coating process monitoring

The accurate measurement of spin orbit torque by utilizing the harmonic longitudinal voltage with Wheatstone bridge structure

Cite as: Appl. Phys. Lett. **116**, 222402 (2020); doi: [10.1063/1.5145221](https://doi.org/10.1063/1.5145221)

Submitted: 17 January 2020 · Accepted: 24 May 2020 ·

Published Online: 2 June 2020



View Online



Export Citation



CrossMark

Bo Wang, Yonghai Guo, Bo Han, Ze Yan, Tao Wang, Dezheng Yang,  Xiaolong Fan,  and Jiangwei Cao ^{a)} 

AFFILIATIONS

Key Laboratory for Magnetism and Magnetic Materials of the Ministry of Education, Lanzhou University, Lanzhou 730000, People's Republic of China

^{a)} Author to whom correspondence should be addressed: caojw@lzu.edu.cn

ABSTRACT

The microscopic mechanism for the current-induced spin-orbit torque (SOT) in magnetic heterostructures is still under debate. The accurate measurement of SOT effective fields and their thickness dependence is the basis for understanding this issue. In this work, we measured the SOT effective fields for Pt/NiFe bilayers by utilizing the harmonic longitudinal voltage (HLV) method with a Wheatstone bridge structure. Benefiting from the elimination of the linear resistance in the bridge structure and the large magnetoresistance difference resulting from the large length-width ratio of the bridge element, we achieved very high measurement accuracy for both field-like and damping-like effective fields in the Pt/NiFe bilayers. On this basis, we demonstrated the possibility of the SOT measurement with a relatively low current density ($\sim 10^9$ A/m²) by utilizing the HLV method with a Wheatstone bridge structure and found that the method we proposed is also applicable to the Pt/CoFeB system with a low anisotropic magnetoresistance ratio.

Published under license by AIP Publishing. <https://doi.org/10.1063/1.5145221>

Current-induced spin-orbit torque (SOT) mediates the transfer of angular momentum from the lattice to the spin system, leading to sustained magnetic oscillations,¹ domain wall motion,^{2,3} or switching of ferromagnetic (FM)^{4,5} and antiferromagnetic structures.^{6,7} Experimentally, SOT can be decomposed into two orthogonal components: damping-like (DL) and field-like (FL) torque.⁸ Besides the potential application of SOT for driving energy-efficient magnetic memory, nano-oscillators, and nonvolatile logic devices, the microscopic mechanism for these torques is a topic of concern, which is still under debate. In ferromagnetic (FM)/nonmagnetic (NM) bilayers, the proposed mechanism for SOT includes the spin Hall effect (SHE)⁹ in the NM layer and the Rashba-Edelstein (RE) effect at the FM/NM interface.¹⁰⁻¹³ Considering the different NM thickness dependence of these effects, analyzing the thickness dependence of DL and FL efficiencies should provide information about the physical origin of the torques. In the simplest theoretical models, effects coming from the interfacial RE interaction should be independent of the NM layer thickness (t_N),¹³ whereas effects emerging from the bulk SHE should scale as $[1 - \text{sech}(t_N/\lambda_{sf})]$ according to the spin drift-diffusion model.^{1,13} Therefore, the exact measurement of SOT fields and their thickness dependence is the basis for solid understanding of their physical mechanism.

Several methods have been proposed to measure the SOT effective fields in FM/NM heterostructures. Among them, the harmonic Hall voltage (HHV) method detects the harmonic Hall response of the magnetization to a low frequency ac.^{14,15} This method has been widely used since it can simultaneously determine the DL and FL torque and current-induced thermoelectric signals.¹⁶⁻¹⁹ However, this method gives low accuracy or even becomes invalid for a FM layer with a low Hall coefficient. On the other hand, the current-induced alternating oscillation of magnetization can also introduce a harmonic signal in longitudinal voltage because of the anisotropic magnetoresistance (AMR) effect and spin Hall magnetoresistance (SMR) effect.²⁰⁻²³ In our previous work, we proposed a new method to compute the corresponding SOT effective fields by using the harmonic longitudinal voltage (HLV) and applied this method to the Pt/NiFe system.²⁴ We found that the HLV method can effectively separate the DL and FL torque, Oersted field, and thermoelectric signal. However, different from HHV, the existence of large linear resistance in the HLV method degrades the measurement accuracy. Specifically for the xz-plane scan of HLV, a large external field is required to overcome the demagnetization field, resulting in a weak harmonic signal. In addition, since the HLV signal is proportional to the square of the applied current, normally, a large current density is required to obtain a sizable harmonic voltage.

Utilizing the Wheatstone bridge structure is an effective method to improve the measurement accuracy for weak signals, which has been recently used for probing the unidirectional magnetoresistance in the FM/NM/Heavy metal structure²⁵ or the nonlinear resistance term induced by the spin torque in a single FM layer.²⁶ In this work, we try to improve the SOT measurement accuracy of the HLV method by utilizing the Wheatstone bridge structure. Because of the elimination of the offset voltage in the bridge structure and the large resistance difference (ΔR) resulting from the large length–width ratio of the bridge element, ultra-high measurement accuracy was achieved for both DL and FL torques in the Pt/NiFe bilayers. In addition, we demonstrated the measurement of SOT at a relatively low current density ($\sim 10^9$ A/m²) for the Pt/NiFe system and found that the method we proposed is also applicable to the Pt/CoFeB system with a low AMR ratio.

We first consider HLV from a Hall bar device. According to Ohm's law, longitudinal voltage V is a product of the resistance R and the current I passed along the device. Taking into account the resistance change resulting from the current-induced effective fields, a nonlinear resistance term should be introduced, i.e.,

$$R = R_0 + R(I) = R_0 + \frac{dR}{dI}I. \quad (1)$$

When a sinusoidal current ($I = I_0 \sin \omega t$) is applied, we have

$$\begin{aligned} V(t) &= R(t)I(t) = \left(R_0 + \frac{dR}{dI}I_0 \sin \omega t \right) I_0 \sin \omega t \\ &= V^0 + V^\omega \sin \omega t - V^{2\omega} \cos 2\omega t, \end{aligned} \quad (2)$$

where $V^0 = \frac{1}{2} \frac{dR}{dI} I_0^2$, $V^\omega = R_0 I_0$, $V^{2\omega} = \frac{1}{2} \frac{dR}{dI} I_0^2$.

Here, we define the second harmonic resistance as

$$R^{2\omega} = \frac{dR}{dI} I_0 = \frac{2V^{2\omega}}{I_0}, \quad (3)$$

where dR/dI can be deduced by considering the expression of AMR and SMR, as well as the current-induced effective fields [including the DL effective field (H_{DL}), FL effective field (H_{FL}), and Oersted field (H_{Oe})]. Combining the harmonic signal resulting from the unidirectional spin Hall magnetoresistance (UMSR)^{27–29} effect in the FM/NM bilayers and that from the thermoelectrical effect [including the anomalous Nernst effect (ANE) and the spin Seebeck effect (SSE)],¹⁷ the angular dependence of the total theoretical $R^{2\omega}$ for the xy - and xz -plane can be expressed as²⁴

$$\begin{aligned} R_{xx}^{2\omega}(\varphi_M) &= -\frac{(R_x - R_y)(H_{FL} + H_{Oe})}{2H} (\sin 3\varphi_M + \sin \varphi_M) \\ &\quad + \alpha \sin \varphi_M, \\ R_{xx}^{2\omega}(\theta_M) &= \frac{(R_x - R_z)H_{DL}}{H_K} \frac{\sin 2\theta_M}{\cos 2\theta_M - \sqrt{\left(\frac{H}{H_K}\right)^2 + \frac{\cos 4\theta_M - 1}{8}}} \\ &\quad + \gamma \nabla T_z \sin 2\theta_M, \end{aligned} \quad (4)$$

where θ_M and φ_M are the polar and azimuthal angles of magnetization, as shown in Fig. 1(b). H and H_K represent the external field during the measurement and the effective out-of-plane anisotropy field of the FM layer, respectively.

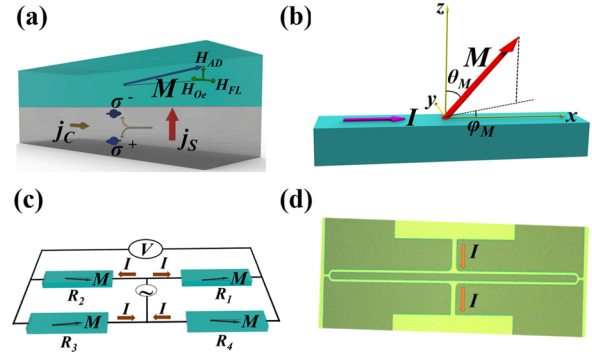


FIG. 1. Schematic illustrations of the current-induced SOT effective fields in FM/NM bilayers (a) and coordinate system (b). (c) and (d) show the schematic and photograph of a Wheatstone bridge structure for the HLV measurement.

In a balanced Wheatstone bridge structure, to keep the same current density as that in the Hall bar devices discussed previously, we consider that a dc $2I$ is applied to two terminals of the bridge along the y axis, as shown in Fig. 1(c), half of the current will flow in each element, and the voltage drop on the adjacent elements cancels each other and contributes zero output voltage. However, considering the nonlinear resistance (i.e., $\frac{dR}{dI}I$) caused by SOT and other effects, the output voltage of the bridge can be written as

$$V_B = V^+ - V^- = I \left(R + \frac{dR}{dI}I \right) - I \left(R - \frac{dR}{dI}I \right) = 2 \frac{dR}{dI} I^2. \quad (6)$$

When a sinusoidal current ($I = 2I_0 \sin \omega t$) is applied, the second harmonic voltage of the bridge is given by

$$V_B^{2\omega}(t) = I_0^2 \frac{dR}{dI} \cos 2\omega t. \quad (7)$$

Therefore, the nonlinear resistance can be obtained from the measured HLV in the bridge structure by $R^{2\omega} = \frac{dR}{dI} I_0 = \frac{V_B^{2\omega}}{I_0^2}$, where $V_B^{2\omega}$ denote the amplitude of the second HLV measured from the bridge structure. By fitting the measured $R^{2\omega}$ by theoretical equations (4) and (5), the current-induced SOT effective fields can be obtained.

We deposited the film stacks on thermally oxidized Si substrates by magnetron sputtering with a base pressure prior to 2×10^{-7} Torr. The detailed film structures are substrate/Ta(1)/Pt(t_{Pt})/Ni₈₀Fe₂₀(6)/MgO(1)/Ta(1) with the t_{Pt} layer varying from 2 nm to 10 nm and substrate/Ta(1)/Pt(t_{Pt})/CoFeB(3)/MgO(1)/Ta(1) (the numbers in the brackets are layer thicknesses in nm), which were thereafter denoted as Pt/NiFe and Pt/CoFeB, respectively. After deposition, the film stacks were subsequently patterned into Hall bar devices ($200 \mu\text{m} \times 10 \mu\text{m}$) and Wheatstone bridge structures (the dimensions for each element are $1000 \mu\text{m} \times 10 \mu\text{m}$) by standard photolithography and ion milling techniques, as shown in Fig. 1(d). The details for the angular-dependent HLV measurement can be found in our previous work.²⁴ However, it should be noted that, due to the elimination of the linear resistance in the bridge structure, the angular dependence of the linear resistance (i.e., R_0 or R^ω) can only be obtained from the Hall bar structure, while the nonlinear resistance ($R^{2\omega}$) can be obtained from both the bridge and Hall bar structures.

Figure 2(a) shows the typical angular dependence of the resistance in the xy - and xz -plane, for the sample with a Pt(5 nm)/NiFe(6 nm) structure. The magnetoresistance (MR) effect in the xz -plane is believed to originate from the AMR of the FM layer, while the MR effect in the xy -plane is the sum of the AMR in the FM layer and the SMR at the FM/NM interface. The notable MR effect in both planes offers the possibility of measuring SOT by utilizing the HLV method. Figure 2(b) presents the typical $R_{xx}^{2\omega}(\varphi_M)$ curves measured from the bridge structure under different external fields H (400 Oe–5 kOe), for the sample with a Pt(5 nm)/NiFe(6 nm) structure. In these curves, we recognize dominant $(\sin 3\varphi + \sin \varphi)$ and $\sin \varphi$ components, which correspond to the first term (contribution of current-induced FL and Oersted field) and the second term (contribution of USMR, ANE, and SSE) in Eq. (4), respectively. By fitting the experimental $R_{xx}^{2\omega}(\varphi_M)$ with the theoretical equation, these two terms can be separated. The coefficients of the $(\sin 3\varphi + \sin \varphi)$ term are presented in the inset of Fig. 2(b), as a function of the inverse of external fields $(1/H)$. It shows a linear dependence on $1/H$, in accordance with our theoretical deduction [Eq. (4)]. Figure 2(c) shows the typical $R_{xx}^{2\omega}(\varphi_M)$ curves measured with different current densities in the Pt layer (j_{Pt}). We note that the amplitude of $R_{xx}^{2\omega}(\varphi_M)$ decrease with decreasing current density and it still shows an observable signal with an enough signal noise ratio (SNR) at relatively low j_{Pt} down to 3.4×10^9 A/m². Figure 2(d) shows the calculated effective fields (H_{eff}) with j_{Pt} varying from 3.4×10^9 A/m² to 5.4×10^{10} A/m². H_{eff} increases from 0.09 Oe to 1.29 Oe, giving a constant H_{eff}/j_{Pt} ratio of 2.6 ± 0.2 Oe per 10^{11} A/m².

The DL torque can be determined from the angular dependence of the harmonic resistance ($R_{xx}^{2\omega}(\theta_M)$) in the xz -plane scan. It should be noted that, for the xz -plane scan, as the effective out-of-plane

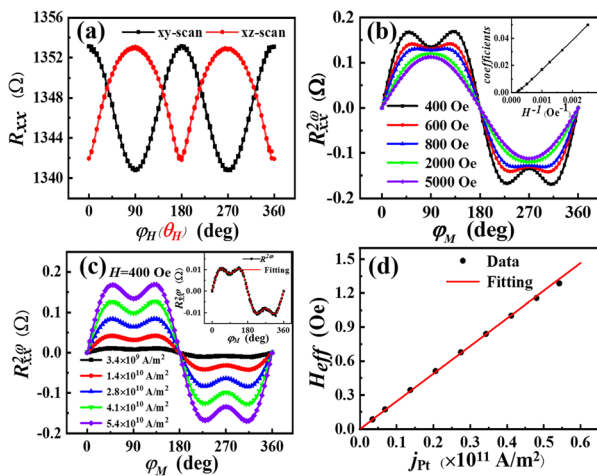


FIG. 2. The harmonics signal and the effective fields measured for the Pt(5)/NiFe(6) bilayer structure. (a) The first harmonic signal measured from the Hall bar structure with the magnetization rotation in the xy - and xz -plane; (b) the second harmonic signal $R_{xx}^{2\omega}(\varphi_M)$ measured from the Wheatstone bridge structure with magnetization rotation in the xy -plane; a constant external field of 400–5 kOe was applied during the measurements, and the current density amplitude in the Pt layer (j_{Pt}) is around 5.4×10^{10} A/m²; the inset shows the coefficients of the $(\sin 3\varphi + \sin \varphi)$ term as a function of $1/H$; (c) $R_{xx}^{2\omega}(\varphi_M)$ curves measured from the Wheatstone bridge structure with $H = 400$ Oe and different j_{Pt} values; (d) the total in-plane transverse effective field ($H_{FL} + H_{Oe}$) as a function of j_{Pt} .

anisotropy field of the Ni₈₀Fe₂₀ layer is comparable to the applied field (10–15 kOe), the moment is not aligned coherently with the field direction in the measurement. Therefore, in the presented figures, we have transformed the measured $R_{xx}^{2\omega}(\theta_H)$ to $R_{xx}^{2\omega}(\theta_M)$ curves by the relationship between θ_M and θ_H , which can be derived from $R_{xx}^{\omega}(\theta_H)$ curves.²⁴ Figure 3(a) shows typical $R_{xx}^{2\omega}(\theta_M)$ curves for the Pt(5 nm)/NiFe(6 nm) sample, measured under the different applied fields of 10–15 kOe. For all $R_{xx}^{2\omega}(\theta_M)$ curves, we note that a distorted $\sin 2\theta$ component dominates the angular dependence, and the amplitude of them decreases with the increasing applied field, in accord with our theoretical expectation. Figure 3(b) shows the typical $R_{xx}^{2\omega}(\theta_M)$ curves measured with different current densities. By fitting the experimental data $R_{xx}^{2\omega}(\theta_M)$ with the theoretical expression [Eq. (5)], the H_{DL} values can be obtained. We reassert that, for the curves measured with lowest $j_{Pt} \sim 3.4 \times 10^9$ A/m², as shown in Fig. 3(c), it still shows observable signals, but much low accuracy than that in the xy -plane, mostly due to the different applied fields for the xy -plane and xz -plane scan. The large applied field during the xz -plane scan suppresses the oscillation of the moment, resulting in a weak harmonic signal. The calculated H_{DL} value is shown in Fig. 3(d) with j_{Pt} varying from 3.4×10^9 A/m² to 6.9×10^{10} A/m². The H_{DL} value increases from ~ 0.3 Oe to ~ 6.0 Oe, giving a constant H_{DL}/j_{Pt} ratio of 9.23 ± 0.09 Oe per 10^{11} A/m².

Then, we discuss the thickness dependence of the FL effective field and DL efficiency in the Pt/NiFe bilayers. It should be noted that the effective fields derived from $R_{xx}^{2\omega}(\varphi_M)$ curves include the FL and Oersted field. After subtracting the Oersted field induced by the current in the Pt layer, which can be calculated as $H_{Oe} = j_{Pt}t_{Pt}/2$, the pure H_{FL} component correlated with spin orbit coupling (SOC) can be obtained. Figure 4(a) shows the thickness dependence of the measured total transverse field and calculated H_{Oe} and H_{FL} for the Pt/NiFe bilayers. In the measured range with $t_{Pt} = 2$ –10 nm, we observe that H_{FL} shows thickness-independent behavior, which may reveal its interface origin induced by the RE effect. Then, we discuss the DL torque in terms of the drift-diffusion approach widely employed in the analysis

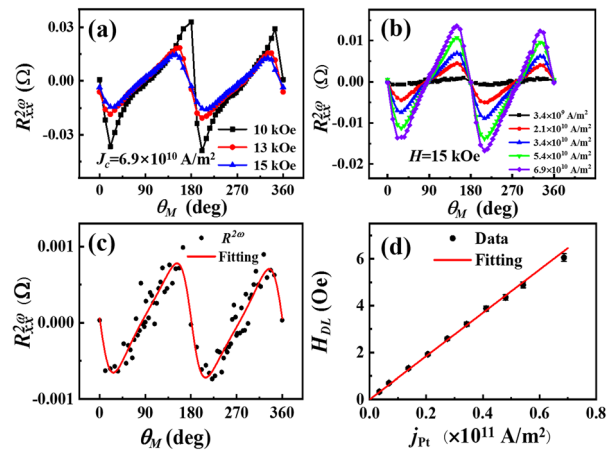


FIG. 3. The angular dependence of the second harmonic signal in the xz -plane ($R_{xx}^{2\omega}(\theta_M)$) measured for the Pt(5)/NiFe(6) bilayer with different external fields (a) and current densities (b); (c) the theoretical fitting of the $R_{xx}^{2\omega}(\theta_M)$ curve measured with the lowest current density ($j_{Pt} = 3.4 \times 10^9$ A/m²) and $H = 15$ kOe; (d) the derived DL effective field as a function of j_{Pt} .

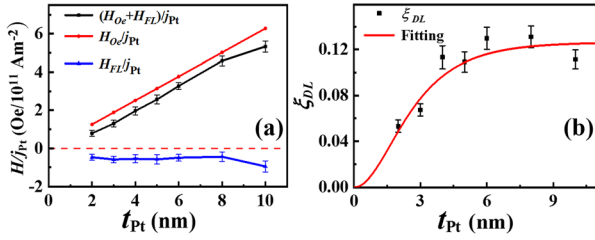


FIG. 4. The Pt thickness dependence of the total transverse effective field: Oersted field and FL field (a) and the DL efficiency (b) for Pt/NiFe samples.

of SOT experiments. The DL efficiency ζ_{DL}^{jPt} was computed by using the following expression: $\zeta_{DL}^{jPt} = \frac{2e}{h} \frac{M_{SFM} H_{DL}}{j_{Pt}}$.³⁰ Assuming that the spin current flowing from the Pt layer into the NiFe layer is unique due to the bulk SHE of Pt and is entirely absorbed at the Pt/NiFe boundary, the simplest drift-diffusion model gives a Pt layer thickness dependence of DL-SOT efficiency $\zeta_{DL}^{jPt} = \theta_{SH} [1 - \text{sech}(\frac{t_{Pt}}{\lambda_S})]$.¹ The fitting to the Pt thickness dependence of ζ_{DL}^{jPt} [Fig. 4(b)] yields an effective spin Hall angle of $\theta_{SH} = 0.126 \pm 0.009$. This value is in the range of previous measured values,^{31–33} but a little bit larger than that measured by the HLV method in Hall bar structures in our previous work. We suggest that this discrepancy may originate from the different properties for two groups of the samples because we obtained a similar θ_{SH} value from the Wheatstone bridge and Hall bar structure for the same group of samples (see the [supplementary material](#) for details). The previous experimental results suggest that the variation of the Pt resistivity among different groups is one of the main reasons for the spread of θ_{SH} values in the literature.³⁴ In this group of samples, a large Pt resistivity ($\sim 44 \mu\Omega \text{ cm}$) was obtained, in comparison with the value ($\sim 27 \mu\Omega \text{ cm}$) in our previous work, resulting in a relatively large θ_{SH} .

Next, we emphasize the high accuracy of the SOT measurement by utilizing the HLV method with a Wheatstone bridge structure. The measured $R_{xx}^{2\omega}(\theta_M)$ curves with the same current density ($j_{Pt} = 4 \times 10^{10} \text{ A/m}^2$) from the bridge and Hall bar devices are shown

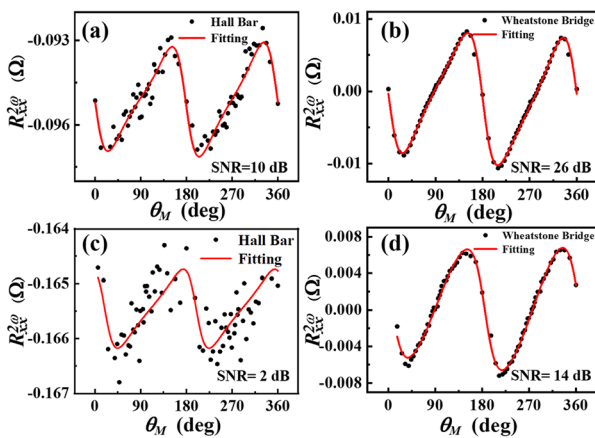


FIG. 5. Comparison of the $R_{xx}^{2\omega}(\theta_M)$ signal measured from the Hall bar and Wheatstone bridge structures, for the samples of Pt(5)/NiFe(6) [(a) and (b)] and Pt(5)/CoFeB(3) [(c) and (d)] bilayers.

TABLE I. The extracted SOT field, spin Hall angle (θ_{SH}) values, and the errors from the two structures for Pt/NiFe and Pt/CoFeB samples.

	H_{DL} (Oe/10 ¹¹ A/m ²)	$H_{FL} + H_{Oe}$ (Oe/10 ¹¹ A/m ²)	θ_{SH}
Pt(5)/NiFe(6) (bridge)	9.23 ± 0.09	2.6 ± 0.2	0.126 ± 0.009
Pt(5)/NiFe(6) (Hall bar)	8.7 ± 0.7	2.5 ± 0.3	0.12 ± 0.02
Pt(5)/CoFeB(3) (bridge)	14 ± 1	-1.6 ± 0.2	0.128 ± 0.002
Pt(5)/CoFeB(3) (Hall bar)	14 ± 4	-1.7 ± 0.3	0.12 ± 0.03

in Fig. 5. We note that the SNR of the curve measured from the Wheatstone bridge is much higher than that from the Hall bar structure. This confirms that the SOT measurement accuracy can be greatly improved by utilizing the Wheatstone bridge structure. We also measured Pt/CoFeB samples as a comparison, and the detailed data of the effective fields are summarized in the [supplementary material](#). Figures 5(c) and 5(d) shows typical $R_{xx}^{2\omega}(\theta_M)$ curves measured from the Hall bar and bridge structure for the Pt(5)/CoFeB(3) sample. Because of the extremely small AMR value of CoFeB (around 0.05% in this sample), $R_{xx}^{2\omega}(\theta_M)$ measured from the Hall bar show a very low SNR (~ 2 dB), whereas by utilizing the Wheatstone bridge structure, the SNR was significantly improved up to 14 dB as shown in Fig. 5(d). Table I lists the extracted SOT effective field and spin Hall angle values from the two structures for Pt/NiFe and Pt/CoFeB samples. We can clearly see that the measurement accuracy of SOT fields and θ_{SH} was greatly improved by utilizing the Wheatstone bridge structure for both groups of samples.

Finally, we discuss the limitation and possible errors of this measurement method. In principle, this method is applicable to any conductive sample with an obvious magnetoresistance effect, which is a common phenomenon in FM materials. In addition, for the sample with large perpendicular anisotropy, a large external field is required for the xy-plane scan to align the moment to in-plane, which will suppress the moment oscillation induced by the SOT effect and, therefore, degrade the measurement accuracy of the transverse field (the sum of FL and Oersted field). As for the errors for this method, we should note that, besides the ordinary errors in the transport measurement, an external error may arise from the indirect estimation of the resistance for each leg due to the inhomogeneity of the films.

In summary, we measured the SOT effective fields and their thickness dependence for Pt/NiFe and Pt/CoFeB bilayers by utilizing the harmonic longitudinal voltage (HLV) method with a Wheatstone bridge structure. The thickness-independent FL effective field in the Pt/NiFe system may reveal its interface origin induced by the RE effect, while the good fitting of DL efficiency with the spin drift-diffusion model confirms the SHE scenario in this structure. More importantly, our results confirm that the harmonic longitudinal voltage (HLV) method with a Wheatstone bridge structure can accurately characterize the SOT in the NM/FM structures, even for the system with an extreme AMR effect.

See the [supplementary material](#) for the SOT effective field values of Pt/CoFeB samples and the theoretical fitting of the DL efficiency of Pt/NiFe and Pt/CoFeB samples.

This work was supported by the National Natural Science Foundation of China (Nos. 11674142 and 51771099), the Natural Science Foundation of Gansu Province, China (Grant No. 18JR3RA299), and the Fundamental Research Funds for the Central Universities (Nos. lzujbky-2018-35 and lzujbky-2017-179).

DATA AVAILABILITY

The data that support the findings of this study are available from the corresponding author upon reasonable request.

REFERENCES

- ¹L. Liu, T. Moriyama, D. C. Ralph, and R. A. Buhrman, *Phys. Rev. Lett.* **106**, 036601 (2011).
- ²S. Emori, U. Bauer, S. M. Ahn, E. Martinez, and G. S. D. Beach, *Nat. Mater.* **12**, 611 (2013).
- ³K. S. Ryu, L. Thomas, S. H. Yang, and S. Parkin, *Nat. Nanotechnol.* **8**, 527 (2013).
- ⁴I. M. Miron, K. Garello, G. Gaudin, P. J. Zermatten, M. V. Costache, S. Auffret, S. Bandiera, B. Rodmacq, A. Schuhl, and P. Gambardella, *Nature* **476**, 189 (2011).
- ⁵L. Liu, O. J. Lee, T. J. Gudmundsen, D. C. Ralph, and R. A. Buhrman, *Phys. Rev. Lett.* **109**, 096602 (2012).
- ⁶P. Wadley, B. Howells, J. Zelezny, C. Andrews, V. Hills, R. P. Campion, V. Novak, K. Olejnik, F. Maccheronzi, S. S. Dhesi, S. Y. Martin, T. Wagner, J. Wunderlich, F. Freimuth, Y. Mokrousov, J. Kunes, J. S. Chauhan, M. J. Grzybowski, A. W. Rushforth, K. W. Edmonds, B. L. Gallagher, and T. Jungwirth, *Science* **351**, 587–590 (2016).
- ⁷S. Y. Bodnar, L. Šmejkal, I. Turek, T. Jungwirth, O. Gomonay, J. Sinova, A. A. Sapozhnik, H. J. Elmers, M. Klau, and M. Jourdan, *Nat. Commun.* **9**, 348 (2018).
- ⁸K. Garello, I. M. Miron, C. O. Avci, F. Freimuth, Y. Mokrousov, S. Blugel, S. Auffret, O. Boulle, G. Gaudin, and P. Gambardella, *Nat. Nanotechnol.* **8**, 587–593 (2013).
- ⁹J. E. Hirsch, *Phys. Rev. Lett.* **83**, 1834 (1999).
- ¹⁰E. van der Bijl and R. A. Duine, *Phys. Rev. B* **86**, 094406 (2012).
- ¹¹V. P. Amin and M. D. Stiles, *Phys. Rev. B* **94**, 104420 (2016).
- ¹²Y. Ou, C. F. Pai, S. Shi, D. C. Ralph, and R. A. Buhrman, *Phys. Rev. B* **94**, 140414(R) (2016).
- ¹³P. M. Haney, H. W. Lee, K. J. Lee, A. Manchon, and M. D. Stiles, *Phys. Rev. B* **87**, 174411 (2013).
- ¹⁴U. H. Pi, K. W. Kim, J. Y. Bae, S. C. Lee, Y. J. Cho, K. S. Kim, and S. Seo, *Appl. Phys. Lett.* **97**, 162507 (2010).
- ¹⁵M. Hayashi, J. Kim, M. Yamanouchi, and H. Ohno, *Phys. Rev. B* **89**, 144425 (2014).
- ¹⁶J. Kim, J. Sinha, M. Hayashi, M. Yamanouchi, S. Fukami, T. Suzuki, S. Mitani, and H. Ohno, *Nat. Mater.* **12**, 240–245 (2013).
- ¹⁷C. O. Avci, K. Garello, M. Gabureac, A. Ghosh, A. Fuhrer, S. F. Alvarado, and P. Gambardella, *Phys. Rev. B* **90**, 224427 (2014).
- ¹⁸X. Qiu, P. Deorani, K. Narayanapillai, K. S. Lee, K. J. Lee, H. W. Lee, and H. Yang, *Sci. Rep.* **4**, 4491 (2014).
- ¹⁹S. Ghosh and A. Manchon, *Phys. Rev. B* **95**, 035422 (2017).
- ²⁰H. Nakayama, M. Althammer, Y. T. Chen, K. Uchida, Y. Kajiwara, D. Kikuchi, T. Ohtani, S. Geprags, M. Opel, S. Takahashi, R. Gross, G. E. Bauer, S. T. Goennenwein, and E. Saitoh, *Phys. Rev. Lett.* **110**, 206601 (2013).
- ²¹Y. T. Chen, S. Takahashi, H. Nakayama, M. Althammer, S. T. B. Goennenwein, E. Saitoh, and G. E. W. Bauer, *Phys. Rev. B* **87**, 144411 (2013).
- ²²J. Kim, P. Sheng, S. Takahashi, S. Mitani, and M. Hayashi, *Phys. Rev. Lett.* **116**, 097201 (2016).
- ²³B. F. Miao, S. Y. Huang, D. Qu, and C. L. Chien, *Phys. Rev. Lett.* **112**, 236601 (2014).
- ²⁴B. Han, B. Wang, Z. Yan, T. Wang, D. Yang, X. Fan, Y. Wang, and J. Cao, *Phys. Rev. Appl.* **13**, 014065 (2020).
- ²⁵C. Lidig, J. Cramer, L. Weißhoff, T. R. Thomas, T. Kessler, M. Kläui, and M. Jourdan, *Phys. Rev. Appl.* **11**, 044039 (2019).
- ²⁶Z. Luo, Q. Zhang, Y. Xu, Y. Yang, X. Zhang, and Y. Wu, *Phys. Rev. Appl.* **11**, 064021 (2019).
- ²⁷C. O. Avci, K. Garello, A. Ghosh, M. Gabureac, S. F. Alvarado, and P. Gambardella, *Nat. Phys.* **11**, 570–575 (2015).
- ²⁸S. S. L. Zhang and G. Vignale, *Phys. Rev. B* **94**, 140411(R) (2016).
- ²⁹I. V. Borisenko, V. E. Demidov, S. Urzhidn, A. B. Rinkevich, and S. O. Demokritov, *Appl. Phys. Lett.* **113**, 062403 (2018).
- ³⁰M. H. Nguyen, D. C. Ralph, and R. A. Buhrman, *Phys. Rev. Lett.* **116**, 126601 (2016).
- ³¹C. F. Pai, Y. Ou, L. H. Vilela-Leão, D. C. Ralph, and R. A. Buhrman, *Phys. Rev. B* **92**, 064426 (2015).
- ³²M. Obstbaum, M. Härtinger, H. G. Bauer, T. Meier, F. Swientek, C. H. Back, and G. Woltersdorf, *Phys. Rev. B* **89**, 060407(R) (2014).
- ³³M. H. Nguyen, C. F. Pai, K. X. Nguyen, D. A. Muller, D. C. Ralph, and R. A. Buhrman, *Appl. Phys. Lett.* **106**, 222402 (2015).
- ³⁴E. Sagasta, Y. Omori, M. Isasa, M. Gradhand, L. E. Hueso, Y. Niimi, Y. Otani, and F. Casanova, *Phys. Rev. B* **94**, 060412 (2016).